8-1-2018

Early detection of fracture failure in SLM AM tension testing with Talbot-Lau neutron interferometry

Adam J. Brooks
Louisiana State University

Hong Yao
Louisiana State University

Jumao Yuan
Louisiana State University

Omoefe Kio
Louisiana State University

Caroline G. Lowery
Louisiana State University

See next page for additional authors

Recommended Citation

Brooks, A., Yao, H., Yuan, J., Kio, O., Lowery, C., Markötter, H., Kardjilov, N., Guo, S., & Butler, L. (2018). Early detection of fracture failure in SLM AM tension testing with Talbot-Lau neutron interferometry. *Additive Manufacturing, 22*, 658-664. https://doi.org/10.1016/j.addma.2018.06.012

Early Detection of Fracture Failure in SLM AM Tension Testing with Talbot-Lau Neutron Interferometry

Adam J. Brooks[a,*], Hong Yao[b], Jumao Yuan[a], Omoefe Kio[a], Caroline G. Lowery[a], Henning Markötter[c], Nikolay Kardjilov[c], Shengmin Guo[b], Leslie G. Butler[a]

[a]*Department of Chemistry, 232 Choppin Hall, Louisiana State University, Baton Rouge, LA 70803, USA*
[b]*Department of Mechanical and Industrial Engineering, Louisiana State University, Baton Rouge, LA 70803, USA*
[c]*Helmholtz Center Berlin for Materials and Energy, 14109 Berlin, Germany*

Abstract

Tensile stress in selective laser melted (SLM) stainless steel 316 (SS316) bars was studied with neutron imaging methods for measurement of attenuation, scattering, and diffraction. The hypotheses for stress failure includes modifications to both the grain structure and residual porosity. Neutron Bragg edge imaging showed a change in crystallographic structure and/or texture at a pre-existing fracture, but did not provide evidence for presumptive crack formation. A Talbot-Lau grating-based neutron interferometer yielded better than 100 μm spatial resolution for the attenuation images and was tuned to an autocorrelation scattering length of 1.97 μm for the dark-field (scattering) images. The interferometry imaging was performed with samples parallel and perpendicular to the linear grating, allowing assessment of scattering along and perpendicular to the additive manufacturing build direction. In the 3D tomography dark-field volume of a tensile stressed bar, features were observed that suggested possible sites of crack formation. The features were quantified with line probes and found to be reproducible over three tomography experiments. After imaging, the half-stressed bar was pulled to failure; the fracture point is correlated with a feature in the line probe having enhanced neutron scattering. Neutron interferometry, particularly the dark-field imaging modality, emerges as a powerful non-destructive method for detecting early crack formation in additive manufactured components.

Keywords: additive manufacturing, neutron interferometry, Bragg edge spectroscopy

1. Introduction

Selective laser melting (SLM) is a powder bed fusion additive manufacturing (AM) technology as per ISO/ASTM 52900 that is under rapid development and offers many challenges and opportunities [1]. Due to the lack of optimization with laser scans and solidification processes, as-fabricated SLM parts usually contain many defects, which can lead to poor mechanical strength and a shortened service life. Extensive

*Corresponding author: Adam J. Brooks, Ajbroo01@gmail.com

literature is available on the study of microstructure and failure/crack growth mechanisms in SLM parts [2–11]. It is well known that SLM processing parameters such as laser power, scanning speed, chamber atmosphere, powder layer thickness, and powder size distribution will impact the microstructure and thus mechanical properties in SLM parts [12–20]. Although common microscopy results (TEM, EBSD, or SEM) can reveal the detailed microstructure [21, 22], these characterization methods are destructive in nature and usually involve lengthy sample preparation stages. Also, these common microscopy methods are unsuitable for in-situ testing under mechanical loadings. With no current non-destructive evaluation (NDE) techniques standardized for AM materials, this study searches for a method to detect the point of failure in AM stainless steel (SS) 316 samples.

There are several X-ray and neutron imaging and diffraction methods applicable for tensile and fatigue measurements. In-situ X-ray tomography at a voxel size of $(1.6\ \mu\text{m})^3$ of SS316 bars under tensile stress showed an increase in detectable voids [23]. However, electron microscopy showed voids produced by damage can have dimensions less than a micron [24]. In-situ crystallography can be highly informative [25], yet the gage volumes are large and scanning across an object is rarely performed [26]. Recent advances in neutron grating-based interferometry [27] offer a route to sub-micron inspection of damage features over a large field-of-view. The imaging modality is called dark-field imaging and is closely related to small angle neutron scattering [28]. Related X-ray imaging experiments have been used to measure sub-micron defects in aluminum welds, both conventional and friction-stirred [29, 30]. Another large field-of-view imaging experiment is neutron Bragg edge imaging, which has been used for mapping torsional strain [31–33] .

Neutron Bragg edge imaging provides one method for obtaining crystallographic information in AM samples. In Bragg edge imaging, a series of monochromatic images are collected at varying wavelengths. At wavelengths defined by Bragg's law, there is an abrupt change in attenuation. In the case of AM SS316 samples, probing the phases of internal components can reveal phase transitions from martensite to austenite under strain and also on a pixel by pixel basis [32, 34, 35]. In combination with neutron dark-field imaging, Bragg edge imaging can explain the crystallographic phase transitions in AM samples.

In this proof-of-principle project, two neutron imaging and one microscopy method are applied to SS316 tensile bars prepared by SLM AM. Prior to imaging, some bars were stressed to 75% to fracture (here referred to as half-life). To examine crystal grain structure at fracture and stress regions, neutron Bragg edge imaging and scanning electron microscopy (SEM) were performed. To examine the microcracks at the fracture and stress regions, neutron dark-field interferometry imaging was performed at one autocorrelation scattering length. A preliminary examination was performed on the effect of plastic deformation in the SLM parts with respect to dark-field imaging direction. Following the neutron imaging studies, scanning electron microscopy was performed at regions of interest identified in the Bragg and dark-field images. The results show, in broad terms, that neutron imaging can be utilized to examine stress fracture in SLM AM. In particular, dark-field interferometry at auto-correlation lengths near 2 μm may show the initial formation of cracks for tensile fracture. Of course, *in situ* neutron interferometry experiments are needed to confirm the correlation of growth of imaging features with eventual fracture. The results also help to define the sample parameters, i.e., composition, building parameters, and thickness, needed for compatibility with the interferometry experiment, in particular, adequate neutron transmission and avoidance of dark-field image

saturation.

2. Experimental

2.1. Selective Laser Melting

A Concept Laser Mlab-cusing-R SLM system was used in this study to prepare rectangular shaped plates with a thickness of 2 mm. Austenitic stainless steel (SS) 316L powders (compositions in Table 1) from Concept-Laser (CL 20ES) were used with Concept-Laser's "Speed-cusing" processing parameters. Upon creation of a computer aided design model of the desired geometry, two-dimensional slice and support structure information is created by AutoFab software for input into the Mlab system. During the build process, the Mlab system is purged with argon (Ar) down to an oxygen level less than 0.7%. For each layer, after lowering the building platform by 25 microns, a re-coater blade moves across the build platform and deposits an even layer of SS 316L powders onto the build platform. After the rectangular plates were built, a Mitsubishi wire EDM machine (MV series) was used to cut out the samples per ASTM E8/E8M–16a (Fig. 1).

Table 1: Compositions of SS316 Powders

Element Symbol	**Cr**	**Ni**	**C**	**Mn**	**Mo**	**Si**	**S**	**P**	**Fe**
%	16.5–18.5	10.0–13.0	0–0.030	0–2.0	2.0–2.5	0–1.0	0–0.030	0–0.045	Balance

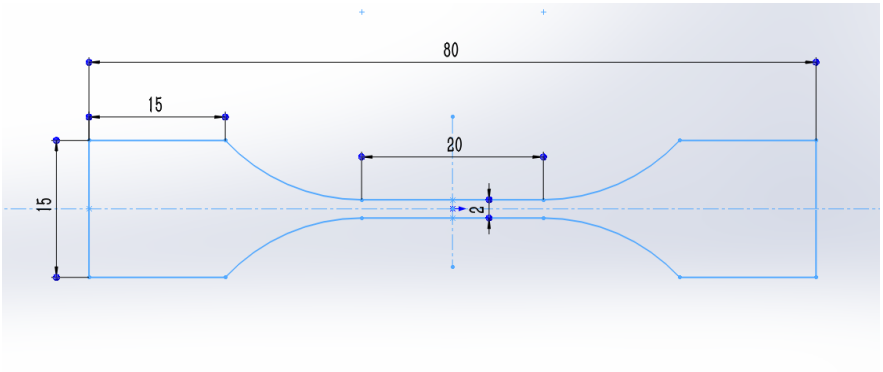

Figure 1: Schematic illustration of a flat tensile bar specimen. All dimensions are in millimeters. The bar thickness is 2 mm.

2.2. Tensile Testing of 2 mm SLM AM Bars

For tensile testing, tensile bar samples with 2×2 mm cross section were tested on an ADMET dual column universal testing machine equipped with a PC based controller at a strain rate of 10^{-4} s^{-1}. The load cell has a capacity of 1000 lbf (model 1210AJ-1K-B). This load cell has a measurement accuracy of +/- 0.5% of reading down to 1/100 of load cell capacity and meets/exceeds ASTM E4, BSENIS 7500-1: 2004, DIN 51221 and JIS B7721 standards. The strain measurement accuracy is +/- 0.5% of reading down to 1/50 of full scale with ASTM E83 class B extensometers, meeting/exceeding ASTM E83 and BSENISO9513: 2002 standards. Mechanical properties of the samples are shown in Table 2.

The sample has a total length of 80 mm, with a uniform test section length of 25 mm. For samples which were pulled until broken, the elongation was found to be around 23% and the tensile strength was larger than 570 MPa (Fig. 2 left). Multiple samples were tested and the elongation at fracture was found to be constant at 23%. A second set of samples were pulled to about 75% elongation before fracture (stressed), Fig. 2 right, and a third type of samples were left in their pristine state.

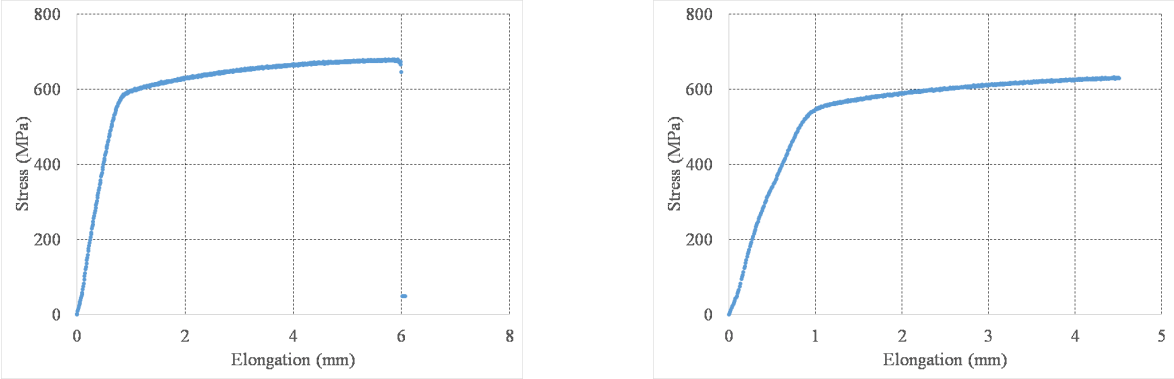

Figure 2: Stress analysis of 2 mm SLM AM tensile bars stressed to failure (left) and stressed to 75% of failure (right).

The design of tensile bar specimen used in this study is based on the Sheet-Type Specimens standard of ASTM E8/E8M-16a. This sheet-type test specimen standard is used for testing metallic materials in the form of a sheet with a nominal thickness ranging from 0.13 mm to 19 mm. The size of the specimen is designed to suit the neutron dark-field interferometry measurements with a multiple sample setup.

2.3. Electron Microscopy Analysis

The microstructure of the tested samples were examined using field-emission scanning electron microscope FE-SEM (FEI, Quanta 3DFEG) equipped with backscattering electron (BSE) and energy dispersive spectroscopy (EDS) detector at LSU Shared Instrumentation Facility (SIF).

For SEM, small sections were cut out of the bar samples using a diamond slow-saw and then mounted into epoxy resin (SamplKwick fast cure acrylic resin, produced by Buehler) for easy handing and retention. The targeted surfaces were subsequently ground by 320, 400, 600, 800 and 1000 grits of SiC sandpapers in sequence, before wet-polished with 6, 3, and 1 μm Al_2O_3 suspensions. The polished samples were etched using aqua regia. After immersing in aqua regia for 20 s at room temperature, the samples were immediately cleaned with water. Typical SLM solidification microstructures were observed in all samples.

2.4. Talbot-Lau Interferometry Radiography and Tomography

Talbot-Lau grating interferometry and Bragg edge imaging was performed at the HZB CONRAD2 imaging beamline. The beamline operated a pinhole of 3 cm providing neutron flux of $2.4x10^7$ n cm^2 s^{-1} at the

Table 2: Mechanical Properties of SLM SS316 AM

Yield Strength	**Tensile Strength**	**Hardness**	**Modulus of Elasticity**	**Elongation**	**Thermal Conductivity**
470 MPa	570 MPa	98 HRB (20 HRC)	200 GPa	>15%	approx. 15 W/mK

detector (5 m, L/D value of 167). An Andor Ikon L-936 camera (2048×2048 pixels, pixel size 30 μm) was used for imaging. The effective pixel size was 30 μm for interferometry, 60 μm with 2×2 binning. A 100 μm thick ^{6}LiF/ZnS scintillator was used to convert neutron flux into visible light. The source grating, G0, had a period of 790 μm with 20 μm Gd, the phase grating, G1, a period of 7.96 μm with 38 μm Si for a π phase shift at 3.5 Å, and the analyzer grating, G2, a period of 4 μm with 10 μm thick Gd. The distance for G0-G2 was 4500 mm, G1-G2 was 22.7 mm (1st Talbot distance for 3.5 Å), and G2-detector was 4 mm [36].

Grating interferometry imaging of the SS316 samples was performed with gratings in a vertical orientation. 2D and 3D datasets of the 2 mm samples were collected: one with the samples in vertical orientation, two with the samples horizontal. Exposure times of 15 seconds provided sufficient flux through the thinner samples. G0 was stepped from 0 mm to 1.2 mm over 12 steps. The tomography was performed with 200 projections over 0° to 180°.

2.5. Dark-field Data Analysis

The intensity of the fringe pattern generated by the gratings evolves with the position of the stepped grating. The intensity can be fitted with a cosine function [37] or its linear expansion [38]:

$$I(x_g) = A + B\cos\left(\frac{2\pi x_g}{p_g} + \phi\right) \tag{1}$$

$$I(x_g) = A + \left[\sin\left(\frac{2\pi x_g}{p_g}\right)\right] B_{cos}\cos\phi + \left[\cos\left(\frac{2\pi x_g}{p_g}\right)\right] B_{sin}\sin\phi \tag{2}$$

$$\text{where } B = \sqrt{B_{cos}^2 + B_{sin}^2} \tag{3}$$

The offset A and amplitude B of Eq. 1 are used to define the the fringe visibility, as visibility = B/A. The image modality called "dark-field" is the ratio of fringe visibility with the sample in the beam versus out of the beam:

$$\text{dark-field} = \frac{\text{visibility}_{sample}}{\text{visibility}_{reference}} = \frac{B_{sample}/A_{sample}}{B_{reference}/A_{reference}} \tag{4}$$

2.5.1. Autocorrelation Length

The dark-field image intensity has been correlated with scattering theory for non-interacting spheres [39–42]. The autocorrelation length gives estimates of particle size and volume fraction as a function of the dark-field signal. The scattering length for the HZB Talbot-Lau interferometer was 1.97 μm for the sample upstream of the G1 grating and is computed by [28, 40]:

$$\xi(z) = \frac{\lambda L_s'}{p_{g1}} \tag{5}$$

$$L_s' = (L_1 + L_2 - L_s)\frac{L_2}{L_1}$$

where the distances are defined in Fig. 1 in Ref [39] with values of L_1=4.5 m, L_2=22.7 mm, p_{g1}=4.0 μm, λ=3.5 Å, and L_s=66 mm.

2.6. Bragg Edge Spectroscopy

Bragg edge imaging was performed with monochromatic beam and 100 second exposures from 2 Å - 4.5 Å by steps of 0.02 Å. The monochromator operated with a bandpass of $\Delta E/E \approx 3\%$. The image contrast-to-noise ratio was increased with 2×2 binning. For the line probes, masks were created in ImageJ starting with binarization and erosion of a transmission image, i.e, the line probe for the fractured tensile bars monitor transmission near the fracture, but omit the air/fracture interface.

2.7. Tomography Reconstruction and Visualization

Tomography reconstruction was done using the Advanced Photon Source TomoPy/ASTRA simultaneous iterative reconstruction technique (SIRT) [43]. Visualization was done using Avizo and Volume Graphics. The attenuation volume was used to generate a binary mask which was applied to the dark-field volume. The visualizations are of dark-field/attenuation. The end points of the fractured sample in the three tomography experiments were used to mutually align the three dark-field/attenuation volumes.

3. Results and Discussion

3.1. SEM of Pristine and Stressed SLM SS316 AM Tensile Bars

The molten track level macroscopic pores are visible in both the as-printed SLM samples and the samples after the tensile induced plastic deformation. The size of the macroscopic pores are generally on the order of a few microns to tens of microns. Using speed-cusing processing parameters, the volumetric percentage of the macroscopic pores is about 3% to 5%, as shown in Fig. 3. The tensile induced plastic deformation makes the molten tracks less visible as seen in Fig. 4. The tensile induced plastic deformation generates different orientations in grain microstructures. The tensile induced plastic deformation refines grains, yielding a finer structure as shown in Fig. 5. Of note is the introduction of 100 nm - 300 nm pores throughout the sub-grain orientation as a function of tensile stress.

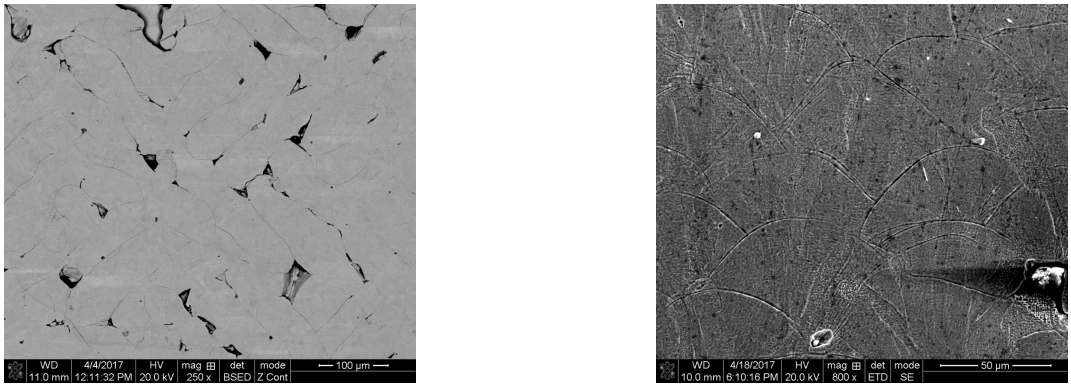

Building plane Cross section

Figure 3: The molten tracks and macroscopic pores on the building plane and cross section of a SLM SS316L part.

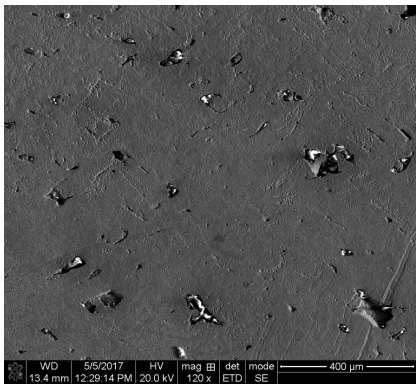

Building plane after tensile testing

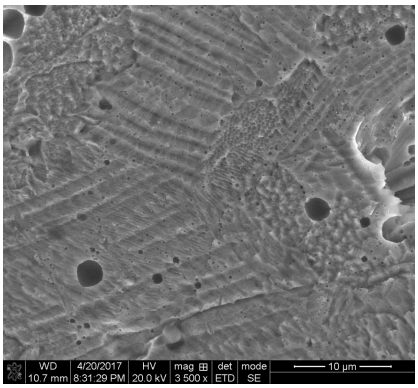

Sub-grain orientations after tensile testing

Figure 4: After tensile testing, the macroscopic pores are visible, however, the molten tracks are harder to identify. Due to plastic deformation, different orientations in sub-grains are clearly visible.

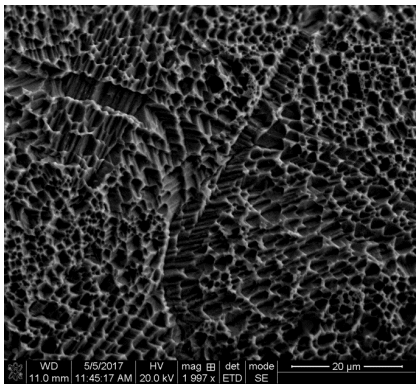

Before tensile testing

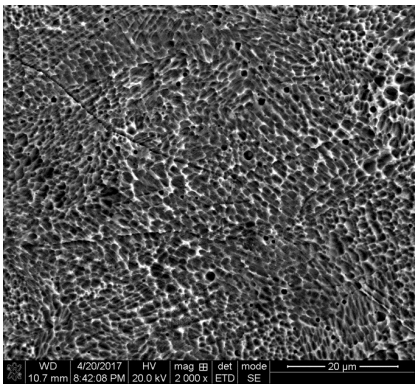

After tensile testing

Figure 5: The etched building plane surface of SLM SS316L parts before (left) and after (right) tensile induced plastic deformation. After tensile induced plastic deformation, the etching pattern shows a finer structure with different orientations.

3.2. Bragg Edge Spectroscopy and Imaging

Neutron Bragg edge imaging is based on wavelength dependent transmission through the sample as governed by Bragg's law,

$$n\,\lambda = 2d_{hkl}sin\theta \tag{6}$$

where neutrons are scattered elastically at various angles, 2θ, from lattice planes at distances, d_{hkl}. Once the scattering angle reaches 180°, $\lambda = 2d_{hkl}$ and backscattering occurs, corresponding to minimal transmission. At wavelengths longer than $2d_{hkl}$, the transmission abruptly increases. In the case of AM imaging, the phase of the SS316 tensile samples was anticipated to be revealed.

Bragg edge imaging results for the SS316 bars are shown in Figs. 6 and 7. Transmission through the fractured sample is the highest, followed by the stressed and pristine samples. Since the fractured bar was pulled the longest of the three bars, it was expected to have the highest transmission due to a thinner path length for the neutrons to penetrate. Also of interest is the region between 3.5 Å - 4.2 Å where a change in texture from pristine to fractured can be observed, consistent with the SEM results in Fig. 5. The pristine

sample has a Bragg edge spectrum characteristic of austenite. This could be related to a transition from γ-austenite (111) at 4.17 Å to α-martensite (110) at 4.10 Å. Previous work has also observed this phase transition in SS316 [32], confirming the validity of the results.

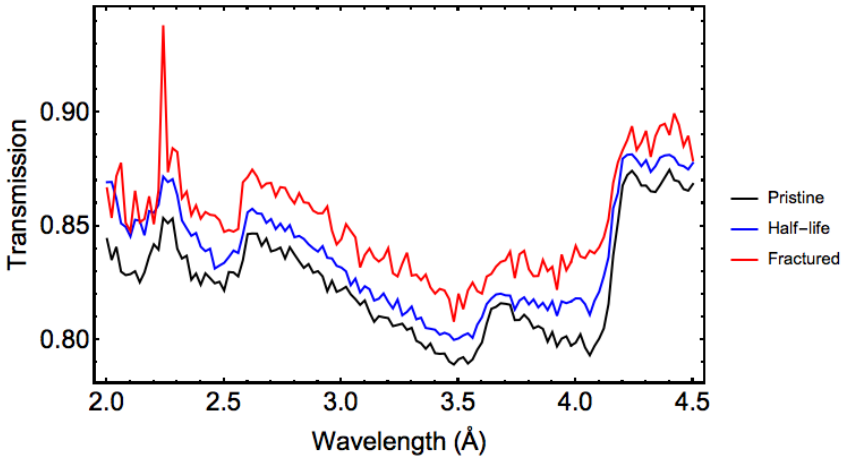

Figure 6: Bragg edge spectra of 2 mm thick SLM SS316L AM samples. The samples subjected to tension, fractured and half-life, show greater neutron transmission, implying the stressed samples are thinner than the pristine sample. The crystal texture change near 4 Å is consistent with the SEM results presented in Fig. 5.

In Fig. 7, the image is obtained by division of the average signal for two wavelength regions, (3.8 Å - 4.1 Å) / (4.3 Å - 4.5 Å). While the scattering is concentrated along the edges of all the samples, the most scattering in the fractured sample can be observed near the crack. In the half life sample, there is a concentrated signal around the x = 12 mm - 15 mm range, the region of the eventual fracture as shown in Fig. 11. However, the signal-to-noise ratio for crack detection is extremely low in this Bragg edge experiment. For this reason, the focus shifted to neutron interferometry and attempts at achieving better contrast from the sample.

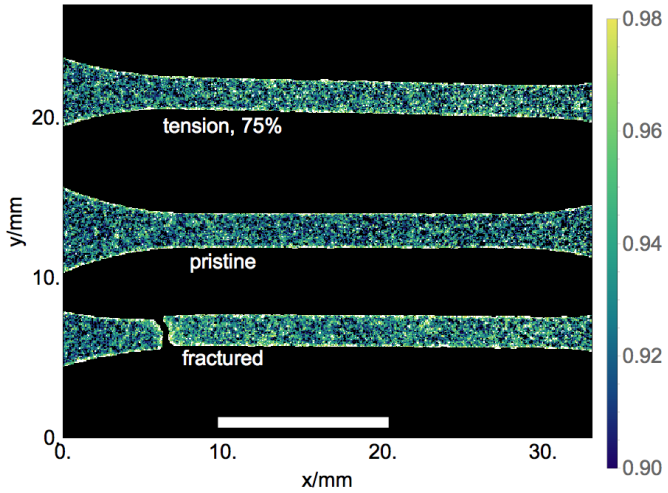

Figure 7: Bragg edge image generated from the same data set presented in Fig. 6. Here, the mean (3.8 Å - 4.1 Å) is divided by mean (4.3 Å - 4.5 Å); the pixel size is 60 μm. Bragg transmission shows a somewhat heterogeneous pristine sample at the sub-mm scale, larger scale changes are seen for the 75% stressed sample, and definite changes are noted near the fracture. The site of presumptive crack formation is not identifiable in the 75% stressed sample.

3.3. Talbot-Lau Interferometry and Tomography

The 2 mm SS316 AM tensile bars were sized to be compatible with interferometry/tomography, in particular, to avoid dark-field saturation with long autocorrelation lengths. The HZB CONRAD2 Talbot-Lau interferometer was configured for ξ=1.97 μm. In search of the optimal sample/interferometer orientation for observation of crack formation, the sample was imaged both parallel and perpendicular to the scattering plane (as defined by the Talbot-Lau gratings). The experiment at the parallel orientation was repeated due to an anticipated low signal-to-noise ratio for the presumptive crack formation. In Expt. 1, the stress axis is perpendicular to the scattering plane (Fig. 8). In Expts. 2 and 3, the stress axis lies in the scattering plane.

Figure 8: The pristine, stressed, and fractured samples before the interferometry/tomography experiment #1. The G1 grating is visible behind the samples. The sample lengths are: pristine (left)- 80 mm, stressed (labeled 3/630)- 83.6 mm, and fractured- 31.45 mm (back) and 54.64 mm (right), 86 mm assembled.

When looking at the reconstructed volumes of the samples, several interesting features were observed (Fig. 9). In the fractured sample, a high amount of scattering (red) can be seen on both sides of the fractured area. In the half-life sample, this scattering occurs along the edges of the neck region. When the sample is rotated 90°, evidence of scattering along the neck edges is minimal. This is indicative of directional scattering from porosity along the print layers. Also of interest is the high amount of scattering at a 45° angle in the half-life sample. The crack in the fractured sample occurs at a 45° angle and although crack formation is expected to occur close to this angle, visualization of this event in a half-life sample before fracture has not been observed until now.

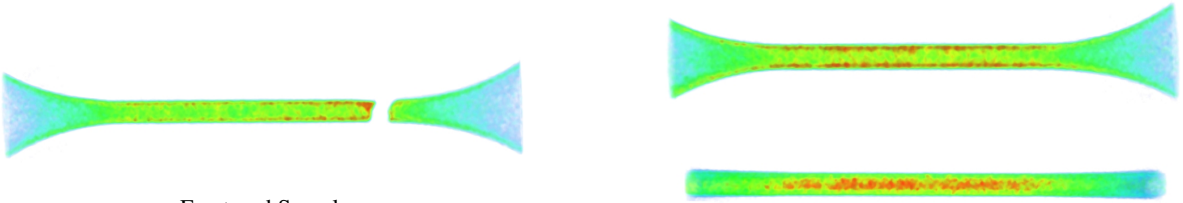

Fractured Sample

Stressed sample

Figure 9: Volume renderings of the fractured (left) and half-life (right) samples. In the image on the right, the top view shows the half-life sample with the build planes horizontal while the bottom view shows the sample sample rotated 90°.

To understand if the scattering at a 45° angle in the half-life sample was accurately represented in the

visualization, line probes for the three experiments were generated (Fig. 10).

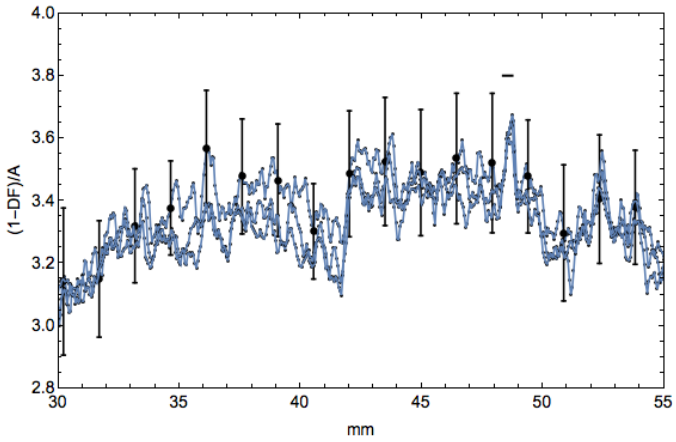

Figure 10: Line probes of the stressed bar from interferometry/tomography experiments #2, #6, and #8. The line-probes use a mask to exclude surface roughness. The horizontal marker at x=48.36±0.7 mm denotes the fracture point of the stressed sample where the uncertainty in position is due to the 1.4 mm stretch between imaging and tensile failure.

The line probes reveals a point at x=48.36±0.7 mm of increased scattering values in the neck region, likely indicative where a point of fracture may be forming. To test if this location is the likely point of fracture, the half-life sample was then stressed to fracture. Figure 11 shows the original stressed sample when fractured.

Figure 11: The stressed sample after additional tensile stress to failure. The sample lengths are 36.64 mm and 48.74 mm (85.0 mm assembled).

Of interest in the now fractured stressed sample is the location of the crack. In comparison to the anticipated fracture location in Fig. 10 (48.36 mm), the crack actually formed at 48.74 mm. As the difference in fracture locations (0.38 mm) is within the standard error, this result indicates the value of neutron interferometry imaging for detecting cracks in stressed samples prior to fracture. With a lack of non-destructive evaluation techniques for additive manufacturing, interferometry serves as a novel method towards visualizing fatigue.

As confirmed in the SEM images, the introduction of 100 nm - 300 nm pores from tensile stress gives a reasonable estimate of what sized features to look for using interferometric imaging. While the autocorrelation length of the instrument, ξ = 1.97 μm, was larger than the SEM features (100 nm - 300 nm), neutron interferometry was still able to show small scattering features that were the location of fracture in large, centimeter sized bars. As the field of AM is focused on observing smaller and smaller defects, new additions like interferometry to traditional CT techniques can shape how AM standards are driven.

4. Conclusions

The first non-destructive neutron imaging experiments of additively manufactured, tensile stressed SS316 bars were performed using Talbot-Lau interferometry and Bragg edge imaging. While the bars were left in their pristine, half-life or fractured states, scattering (dark-field) images from the interferometry experiment showed crack location in a stressed sample before fracture. When the stressed sample was pulled to fracture, the actual crack location was confirmed to be the same as obtained from the imaging experiments. With few non-destructive evaluation techniques for AM parts, this is the first known experiment using neutron interferometry imaging to predict and observe crack location before occurrence.

While there are clear advantages to grating-based interferometry, there are also several limitations. Gadolinium sputtering to produce neutron source and absorption gratings is not easy, resulting in limited grating availability around the world (roughly 10 sets of neutron gratings for Talbot-Lau interferometry). Neutrons are more costly to use than X-rays, hence the trend of higher energy X-ray CT systems capable of penetrating thick metal samples. In the case of several centimeter thick metal samples like SS316, the dark-field signal can saturate at low X-ray energies. Of the pristine SS316 samples studied so far, 2 mm to 3 mm is an optimal thickness. With hot isostatic processing, larger samples may be imaged but there is no data as of yet. With all of these problems in mind, a new approach to interferometry uses a far-field design [37], where only two phase gratings are utilized, meaning a reduction in exposure time due to a decrease in beam absorption. The far-field interferometer can also probe a wide range of autocorrelation lengths, from roughly 50 nanometers up to 5 micrometers. If an AM user knows a rough estimate of a fracture location or pore size, they can tune the instrument to their benefit.

Although particle size information is valuable for neutron interferometry and SEM, there is a need for an analytic chemical method like Bragg edge imaging to provide a detailed analysis of the SS316 AM parts. In comparison to interferometry, Bragg edge imaging revealed a gradual phase change from 3.8 Å - 4.1 Å for the pristine, stressed, and fractured samples. The pristine sample appears to be of the austenite phase, however after pulling of the samples to 75% elongation and fracture, there were indications of a crystallographic phase change towards the α-martensite phase. With the neutron interferometry, Bragg edge, and SEM images presented here, information regarding particle size, phase, and pore location in SLM samples can all be achieved non-destructively. With no standards currently set for the additive manufacturing field, new non-destructive imaging techniques like Talbot-Lau interferometry show promise towards future crack formation prediction and observation before fracture.

Acknowledgments

AJM and LGB gratefully acknowledge support from the Louisiana Consortium for Neutron Scattering (LaCNS), funded by the US Department of Energy-EPSCoR Cooperative Agreement No. EPS-1003897 and the Louisiana Board of Regents. AJB also thanks the Charles E. Coates Memorial Fund for research travel support.HY and SMG are supported by the NSF EPSCoR CIMM project under award OIA-1541079. The use of the CIMM Core User Facilities (CUFs), including LSU Shared Instrumentation Facility (SIF) and Materials Manufacturing, Testing and Evaluation Facility (M2TEF), is acknowledged.

References

[1] Santos, E.C., Shiomi, M., Osakada, K., Laoui, T. (2006) Rapid manufacturing of metal components by laser forming. International Journal of Machine Tools & Manufacture **46**(12-13): 1459–1468.

[2] Olakanmi, E., Cochrane, R., Dalgarno, K. (2015) A review on selective laser sintering/melting (sls/slm) of aluminium alloy powders: Processing, microstructure, and properties. Progress in Materials Science **74**: 401 – 477.

[3] Brandl, E., Heckenberger, U., Holzinger, V., Buchbinder, D. (2012) Additive manufactured alsi10mg samples using selective laser melting (slm): Microstructure, high cycle fatigue, and fracture behavior. Materials & Design **34**: 159 – 169.

[4] Krakhmalev, P., Fredriksson, G., Yadroitsava, I., Kazantseva, N., du Plessis, A., Yadroitsev, I. (2016) Deformation behavior and microstructure of ti6al4v manufactured by slm. Physics Procedia **83**: 778 – 788. Laser Assisted Net Shape Engineering 9 International Conference on Photonic Technologies Proceedings of the LANE 2016 September 19-22, 2016 Frth, Germany.

[5] Gu, D., Hagedorn, Y.C., Meiners, W., Meng, G., Batista, R.J.S., Wissenbach, K., Poprawe, R. (2012) Densification behavior, microstructure evolution, and wear performance of selective laser melting processed commercially pure titanium. Acta Materialia **60**(9): 3849 – 3860.

[6] Vrancken, B., Thijs, L., Kruth, J.P., Humbeeck, J.V. (2012) Heat treatment of ti6al4v produced by selective laser melting: Microstructure and mechanical properties. Journal of Alloys and Compounds **541**: 177 – 185.

[7] Chlebus, E., KuÅnicka, B., Kurzynowski, T., DybaÅa, B. (2011) Microstructure and mechanical behaviour of ti6al7nb alloy produced by selective laser melting. Materials Characterization **62**(5): 488 – 495.

[8] Vrancken, B., Thijs, L., Kruth, J.P., Humbeeck, J.V. (2014) Microstructure and mechanical properties of a novel titanium metallic composite by selective laser melting. Acta Materialia **68**: 150 – 158.

[9] Prashanth, K., Scudino, S., Klauss, H., Surreddi, K., Lber, L., Wang, Z., Chaubey, A., Khn, U., Eckert, J. (2014) Microstructure and mechanical properties of al12si produced by selective laser melting: Effect of heat treatment. Materials Science and Engineering: A **590**: 153 – 160.

[10] Rosenthal, I., Stern, A., Frage, N. (Dec 2014) Microstructure and mechanical properties of alsi10mg parts produced by the laser beam additive manufacturing (am) technology. Metallography, Microstructure, and Analysis **3**(6): 448–453.

[11] Rafi, H.K., Karthik, N.V., Gong, H., Starr, T.L., Stucker, B.E. (Dec 2013) Microstructures and mechanical properties of ti6al4v parts fabricated by selective laser melting and electron beam melting. Journal of Materials Engineering and Performance **22**(12): 3872–3883.

[12] Jia, Q., Gu, D. (2014) Selective laser melting additive manufacturing of inconel 718 superalloy parts: Densification, microstructure and properties. Journal of Alloys and Compounds **585**: 713 – 721.

[13] Olakanmi, E. (2013) Selective laser sintering/melting (sls/slm) of pure al, almg, and alsi powders: Effect of processing conditions and powder properties. Journal of Materials Processing Technology **213**(8): 1387 – 1405.

[14] Strößner, J., Terock, M., Glatzel, U. Mechanical and microstructural investigation of nickelbased superalloy in718 manufactured by selective laser melting (slm). Advanced Engineering Materials **17**(8): 1099–1105.

[15] Kunze, K., Etter, T., Grässlin, J., Shklover, V. (2015) Texture, anisotropy in microstructure and mechanical properties of in738lc alloy processed by selective laser melting (slm). Materials Science and Engineering: A **620**: 213 – 222.

[16] Carter, L.N., Martin, C., Withers, P.J., Attallah, M.M. (2014) The influence of the laser scan strategy on grain structure and cracking behaviour in slm powder-bed fabricated nickel superalloy. Journal of Alloys and Compounds **615**: 338 – 347.

[17] Wang, Z., Guan, K., Gao, M., Li, X., Chen, X., Zeng, X. (2012) The microstructure and mechanical properties of deposited-in718 by selective laser melting. Journal of Alloys and Compounds **513**: 518 – 523.

[18] Kadkhodapour, J., Montazerian, H., Darabi, A., Anaraki, A., Ahmadi, S., Zadpoor, A., Schmauder, S. (2015) Failure mechanisms of additively manufactured porous biomaterials: Effects of porosity and type of unit cell. Journal of the Mechanical Behavior of Biomedical Materials **50**: 180 – 191.

[19] Riemer, A., Leuders, S., Thne, M., Richard, H., Trster, T., Niendorf, T. (2014) On the fatigue crack growth behavior in 316l stainless steel manufactured by selective laser melting. Engineering Fracture Mechanics **120**: 15 – 25.

[20] Hooreweder, B.V., Moens, D., Boonen, R., Kruth, J., Sas, P. Analysis of fracture toughness and crack propagation of ti6al4v produced by selective laser melting. Advanced Engineering Materials **14**(12): 92–97.

[21] Spierings, A., Dawson, K., Dumitraschkewitz, P., Pogatscher, S., Wegener, K. (2018) Microstructure characterization of slm-processed al-mg-sc-zr alloy in the heat treated and hiped condition. Additive Manufacturing **20**: 173 – 181.

[22] Tucho, W.M., Lysne, V.H., Austb, H., Sjolyst-Kverneland, A., Hansen, V. (2018) Investigation of effects of process parameters on microstructure and hardness of slm manufactured ss316l. Journal of Alloys and Compounds **740**: 910 – 925.

[23] Fabrgue, D., Landron, C., Bouaziz, O., Maire, E. (2013) Damage evolution in twip and standard austenitic steel by means of 3d x ray tomography. Materials Science and Engineering: A **579**: 92–98.

[24] Besserer, H.B., Gerstein, G., Maier, H.J., Nurnberger, F. (2016) Specimen preparation by ion beam slope cutting for characterization of ductile damage by scanning electron microscopy. Microscopy Research and Technique **79**(4): 321–327.

[25] Wu, Y., Liu, W.H., Wang, X.L., Ma, D., Stoica, A.D., Nieh, T.G., He, Z.B., Lu, Z.P. (2014) In-situ neutron diffraction study of deformation behavior of a multi-component high-entropy alloy. Applied Physics Letters **104**(5): art. no. 051910.

[26] Santisteban, J.R., Daymond, M.R., James, J.A., Edwards, L. (2006) Engin-x: a third-generation neutron strain scanner. Journal of Applied Crystallography **39**: 812–825.

[27] Pfeiffer, F., Grunzweig, C., Bunk, O., Frei, G., Lehmann, E., David, C. (2006) Neutron phase imaging and tomography. Physical Review Letters **96**(21): art. no. 215505.

[28] Strobl, M., Sales, M., Plomp, J., Bouwman, W.G., Tremsin, A.S., Kaestner, A., Pappas, C., Habicht, K. (2015) Quantitative neutron dark-field imaging through spin-echo interferometry. Scientific Reports **5**: art. no. 16576.

[29] Revol, V., Jerjen, I., Kottler, C., Schutz, P., Kaufmann, R., Luthi, T., Sennhauser, U., Straumann, U., Urban, C. (2011) Sub-pixel porosity revealed by x-ray scatter dark field imaging. Journal of Applied Physics **110**(4): art. no. 044912.

[30] Egan, C.K., Jacques, S.D.M., Connolley, T., Wilson, M.D., Veale, M.C., Seller, P., Cernik, R.J. (2014) Dark-field hyperspectral x-ray imaging. Proceedings of the Royal Society a-Mathematical Physical and Engineering Sciences **470**(2165): art. no. 20130629.

[31] Steuwer, A., Santisteban, J.R., Withers, P.J., Edwards, L., Fitzpatrick, M.E. (2003) In situ determination of stresses from time-of-flight neutron transmission spectra. Journal of Applied Crystallography **36**: 1159–1168.

[32] Woracek, R., Penumadu, D., Kardjilov, N., Hilger, A., Boin, M., Banhart, J., Manke, I. (2014) 3d mapping of crystallographic phase distribution using energy-selective neutron tomography. Advanced Materials **26**(24): 4069–4073.

[33] Dabah, E., Pfretzschner, B., Schaupp, T., Kardjilov, N., Manke, I., Boin, M., Woracek, R., Griesche, A. (2017) Time-resolved bragg-edge neutron radiography for observing martensitic phase transformation from austenitized super martensitic steel. Journal of Materials Science **52**(6): 3490–3496.

[34] Dabah, E., Pfretzschner, B., Schaupp, T., Kardjilov, N., Manke, I., Boin, M., Woracek, R., Griesche, A. (2017) Time-resolved bragg-edge neutron radiography for observing martensitic phase transformation from austenitized super martensitic steel. J. Mater. Sci. **52**(6): 3490–3496.

[35] Woracek, R., Penumadu, D., Kardjilov, N., Hilger, A., Strobl, M., Wimpory, R.C., Manke, I., Banhart, J. (2011) Neutron bragg-edge-imaging for strain mapping under in situ tensile loading. Journal of Applied Physics **109**(9): art. no. 093506.

[36] Manke, I., Kardjilov, N., Schafer, R., Hilger, A., Strobl, M., Dawson, M., Grunzweig, C., Behr, G., Hentschel, M., David, C., Kupsch, A., Lange, A., Banhart, J. (2010) Three-dimensional imaging of magnetic domains. Nature Communications **1**: art. no. 125.

[37] Pushin, D.A., Sarenac, D., Hussey, D.S., Miao, H., Arif, M., Cory, D.G., Huber, M.G., Jacobson, D.L., LaManna, J.M., Parker, J.D., Shinohara, T., Ueno, W., Wen, H. (2017) Far-field interference of a neutron white beam and the applications to noninvasive phase contrast imaging. Phys. Rev. A **95**: art. no. 043637.

[38] Marathe, S., Assoufid, L., Xiao, X., Ham, K., Johnson, W.W., Butler, L.G. (2014) Improved algorithm for processing grating-based phase contrast interferometry image sets. Review of Scientific Instruments **85**(1): art. no. 013704.

[39] Strobl, M. (2014) General solution for quantitative dark-field contrast imaging with grating interferometers. Scientific Reports **4**: art. no. 7243.

[40] Lynch, S.K., Pai, V., Auxier, J., Stein, A.F., Bennett, E.E., Kemble, C.K., Xiao, X., Lee, W.K., Morgan, N.Y., Wen, H.H. (2011) Interpretation of dark-field contrast and particle-size selectivity in grating interferometers. Applied Optics **50**(22): 4310–4319.

[41] Betz, B., Harti, R.P., Strobl, M., Hovind, J., Kaestner, A., Lehmann, E., Van Swygenhoven, H., Gruenzweig, C. (2015) Quantification of the sensitivity range in neutron dark-field imaging. Review of Scientific Instruments **86**(12): art. no. 123704.

[42] Prade, F., Yaroshenko, A., Herzen, J., Pfeiffer, F. (2015) Short-range order in mesoscale systems probed by x-ray grating interferometry. Europhysics Letters **112**(6): art. no. 68002.

[43] Pelt, D.M., Gursoy, D., Palenstijn, W.J., Sijbers, J., De Carlo, F., Batenburg, K.J. (2016) Integration of tomopy and the astra toolbox for advanced processing and reconstruction of tomographic synchrotron data. Journal of Synchrotron Radiation **23**: 842–849.